arXive速報Seminar

2024/10/25 古屋 玲 (徳島大学)

#GAEP1004-10 1-70

The Metallicity Mapping of the Ionized Diffuse Gas at the Milky Way Disk-halo Interface

Bo-Eun Choi [1], Jessica K. Werk [1], Kirill Tchernyshyov [1], J. Xavier Prochaska [2,3,4], Yong Zheng [5], Mary E. Putman [6], Drummond B. Fielding [7,8] and Jay Strader [9]

[1] *Department of Astronomy, University of Washington, Seattle, WA 98195, USA*
[2] *Department of Astronomy and Astrophysics, University of California, Santa Cruz, CA 95064, USA*
[3] *Kavli Institute for the Physics and Mathematics of the Universe (Kavli IPMU), 5-1-5 Kashiwanoha, Kashiwa, 277-8583, Japan*
[4] *Division of Science, National Astronomical Observatory of Japan, 2-21-1 Osawa, Mitaka, Tokyo 181-8588, Japan*
[5] *Department of Physics, Applied Physics and Astronomy, Rensselaer Polytechnic Institute, Troy, NY 12180*
[6] *Department of Astronomy, Columbia University, New York, NY 10027, USA*
[7] *Department of Astronomy, Cornell University, Ithaca, NY 14853, USA*
[8] *Center for Computational Astrophysics, Flatiron Institute, 162 Fifth Avenue, New York, NY 10010, USA*
[9] *Center for Data Intensive and Time Domain Astronomy, Department of Physics and Astronomy, Michigan State University, East Lansing, MI 48824, USA*

ABSTRACT

Metals in the diffuse, ionized gas at the boundary between the Milky Way's interstellar medium (ISM) and circumgalactic medium (CGM), known as the disk-halo interface (DHI), are valuable tracers of the feedback processes that drive the Galactic fountain. However, metallicity measurements in this region are challenging due to obscuration by the Milky Way ISM and uncertain ionization corrections that affect the total hydrogen column density. In this work, we constrain the ionization corrections to neutral hydrogen column densities using precisely measured electron column densities from the dispersion measure of pulsars that lie in the same globular clusters as UV-bright targets with high-resolution absorption spectroscopy. We address the blending of absorption lines with the ISM by jointly fitting Voigt profiles to all absorption components. We present our metallicity estimates for the DHI of the Milky Way based on detailed photoionization modeling to the absorption from ionized metal lines and ionization-corrected total hydrogen columns. Generally, the gas clouds show a large scatter in metallicity, ranging between $0.04 - 3.2\ Z_\odot$, implying that the DHI consists of a mixture of gaseous structures having multiple origins. We estimate the inflow and outflow timescales of the DHI ionized clouds to be $6 - 35$ Myr. We report the detection of an infalling cloud with super-solar metallicity that suggests a Galactic fountain mechanism, whereas at least one low-metallicity outflowing cloud ($Z < 0.1\ Z_\odot$) poses a challenge for Galactic fountain and feedback models.

銀河系のDHIに対して,

1. パルサーDMで$N_{\rm e}^{\rm total}$
2. 紫外線吸収スペクトルから金属イオンのN
3. 光イオン化モデルで銀河系ISMとターゲット雲の電子密度を分離
4. 金属量推定
5. DHI中の構成雲の運動をモデル推定
6. さまざまな金属量のDHI構成ガスが銀河系内の物質循環とCGMとの物質交換に果たす役割を議論

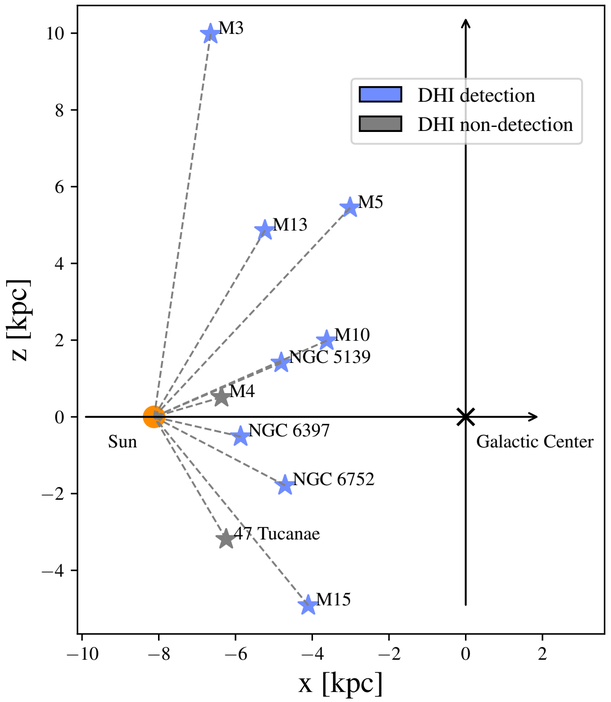

(a) XZ plane

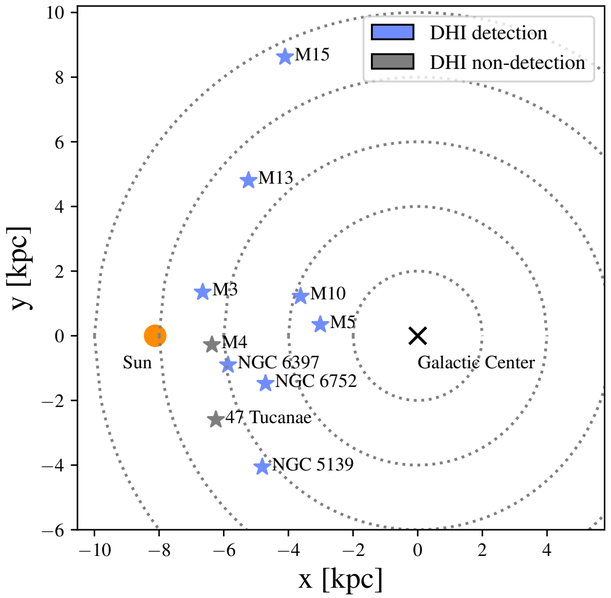

(b) XY plane

Figure 1. 3D distribution of the targeted GCs in the Galactocentric system where the Galactic center lies at (0, 0, 0) kpc and the Sun is at (-8.122, 0, 0) kpc. We mark the GC sight lines where IVCs or/and HVCs are detected in the UV spectrum as "DHI detection" (blue star). A "DHI non-detection" (gray star) indicates that gas kinematically distinct from the Milky Way ISM was not present in the spectrum.

GCとは，球状星団

注意：矢印はHIの視線速度

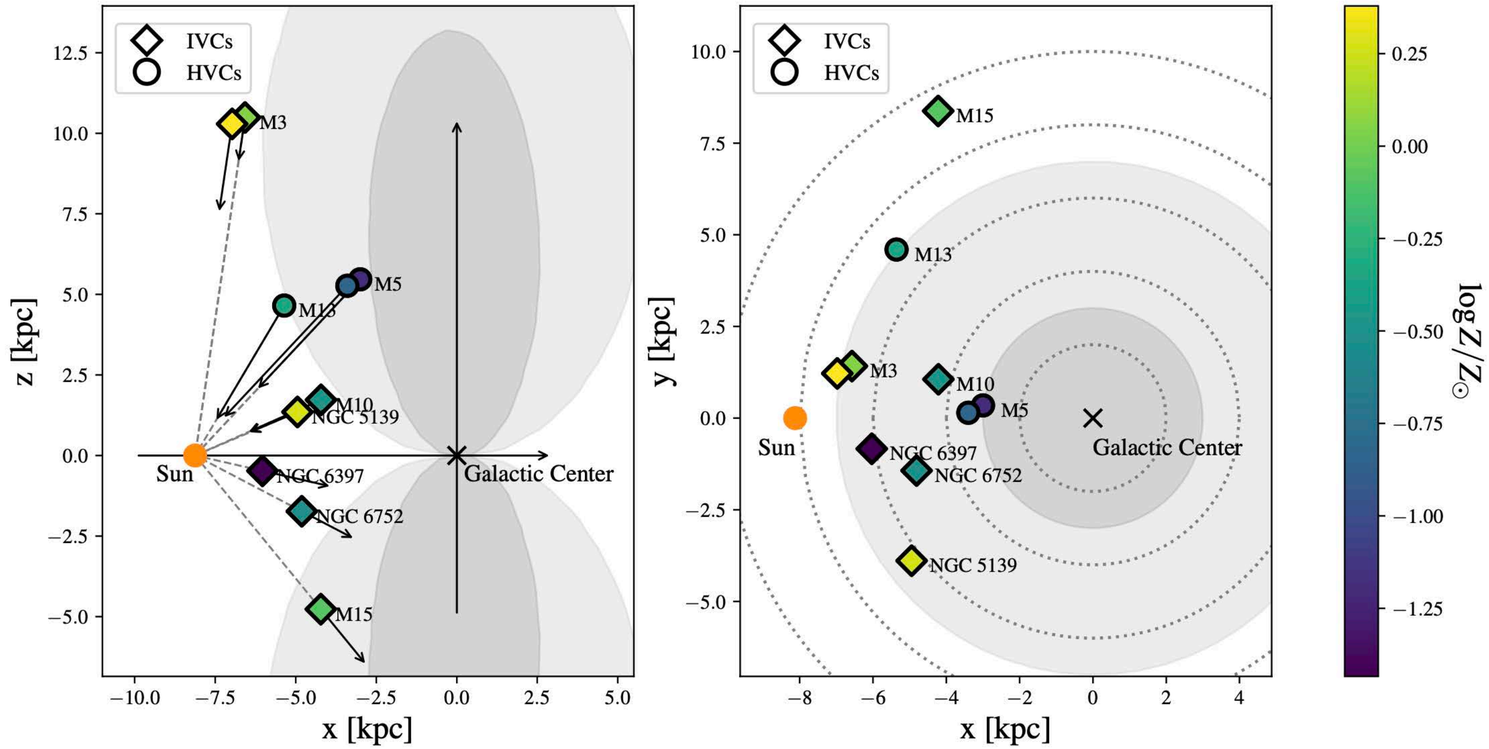

Figure 10. The detected IVCs (diamond) and HVCs (circle) in the Galactocentric system where the Sun is at (-8.122, 0, 0) kpc. The left panel shows the distribution in the XZ plane and the right panel is for the XY plane. We show our metallicity estimation in color. The vector sizes are proportional to the line of sight velocity centroids in the LSR. We also present th Fermi (dark gray-shaded) and eROSITA bubbles (gray-shaded) with their approximate size (Predehl et al. 2020).

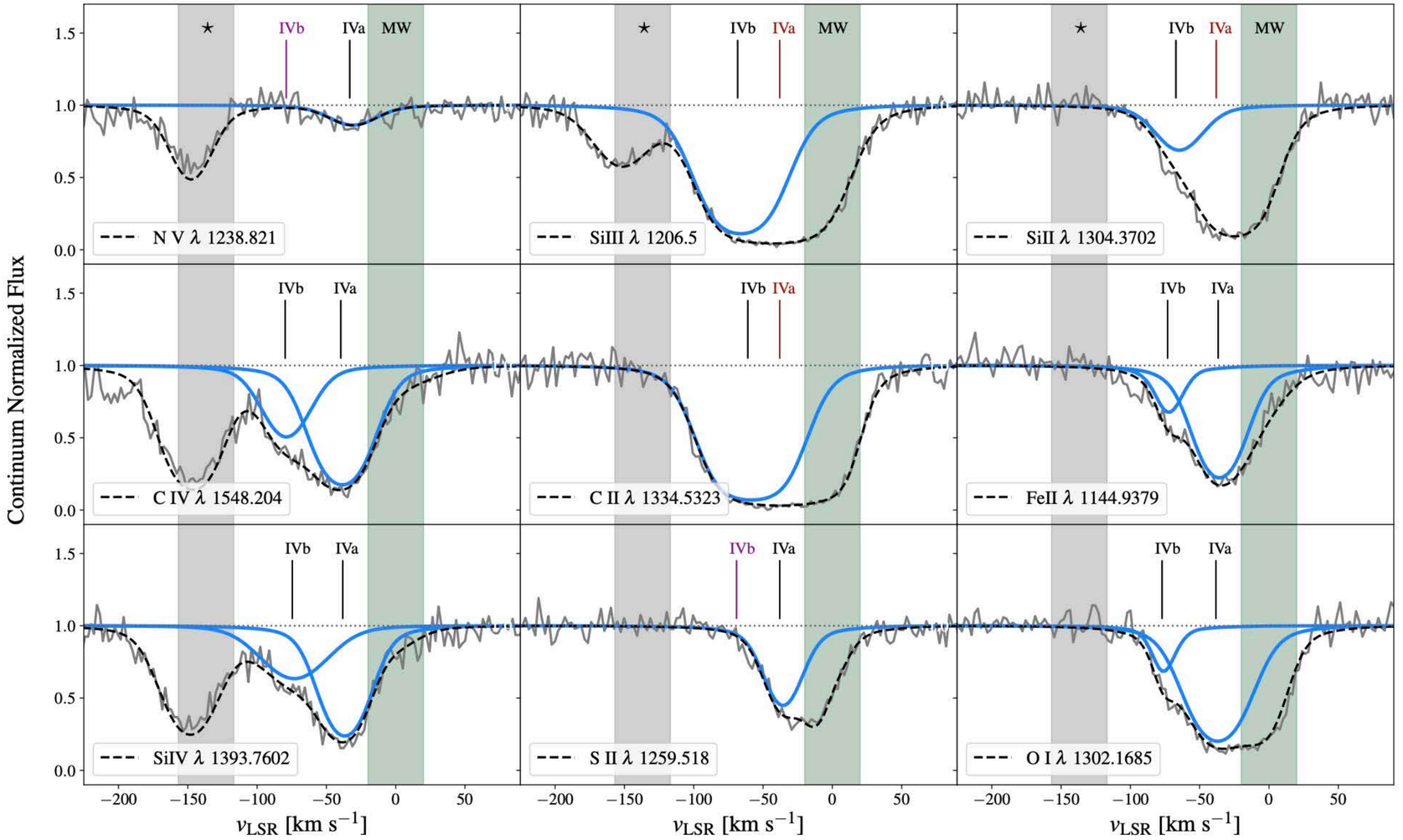

Figure 2. The Voigt profile fit for the M3 sight line (NGC5272-ZNG1). The Black dashed line shows the joint fit including all the absorption components. We separate two intermediate velocity gas clouds, IVa and IVb (blue-solid lines), from the Milky Way ISM (green-shaded) and star (gray-shaded). The component labeled IVa is well-detected in highly-ionized metal species, but is severely blended with saturated absorption from the Milky Way in a few low-ionization metal species (red labels), which makes it impossible to constrain gas column densities from those absorption lines. We mark IVC non-detections in a given ion species with a purple label.

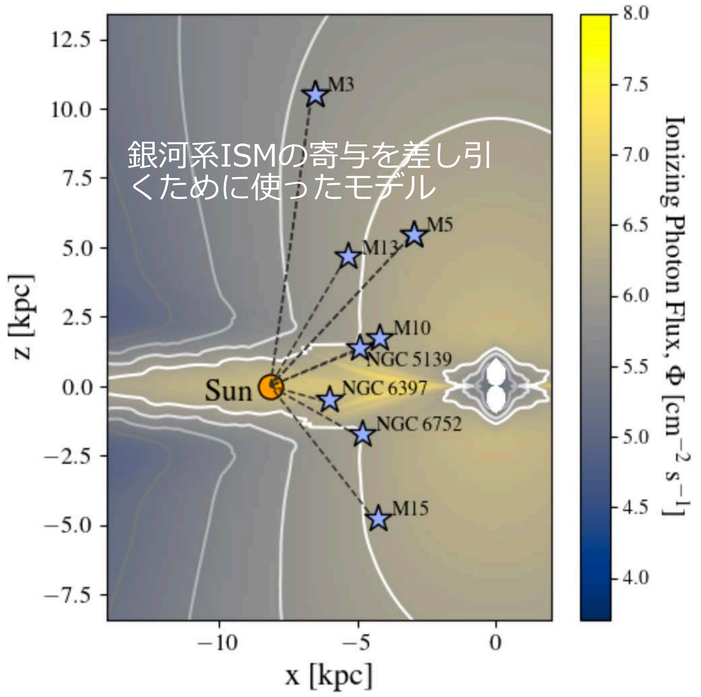

Figure 3. The Milky Way radiation field modeled by Fox et al. (2005), with the positions in xz space of our 8 targets marked by blue stars. The color scale indicates the level of the assumed ionizing photon flux, Log Φ, in units of photons cm^{-2} s^{-1}.

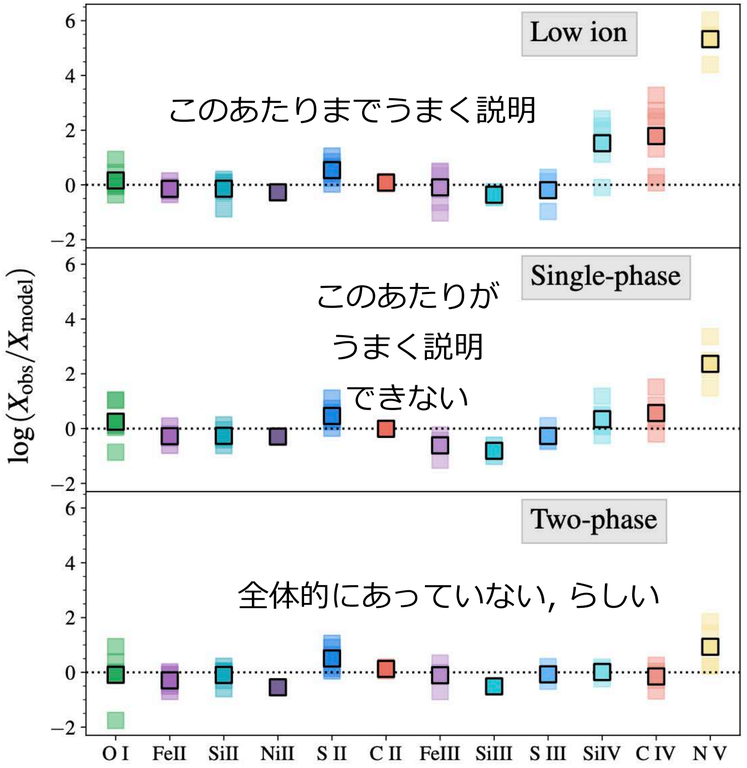

Figure 8. The deviation of the ionic column densities derived from the UV absorption observations from the values derived using best-fit Cloudy model. Ions are ordered on the x-axis in order of increasing ionization potential energy. Median deviations for every cloud are shown with a black box outline. While the low-ion model does not use the observational constraints on N_{SiIV}, N_{CIV}, or N_{NV}, both the single-phase and two-phase models do.

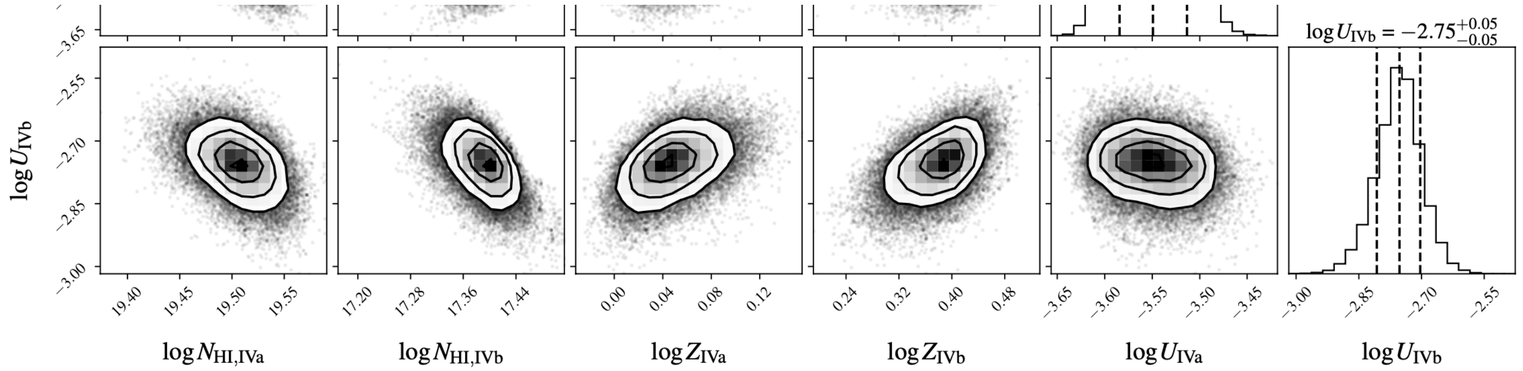

Figure 5. The HMC corner plot of M3 fitting to the photoionized low-ion cloud model. The fitted parameters are neutral hydrogen column density N_{HI}, metallicity $Z/Z_{\odot}$, and ionization parameter U. The median values of posteriors for each IVC are presented with $\pm 1\sigma$.

光イオン化モデリングの結果

CLOUDYを使用して, 以下の3つの想定で観測を再現できるかをテスト.

- **低イオン」モデル**：”低イオン”が光イオン化ガス相に存在し, 中間および高イオンが衝突イオン化されている場合 (結局, このモデルがベストと判断)
- **単相モデル**：すべてのイオンが単一ガス相内で均一に光イオン化されている
- **二相モデル**：すべてのイオンが光イオン化されているが, 雲が2つの異なる密度相に構造化されている場合

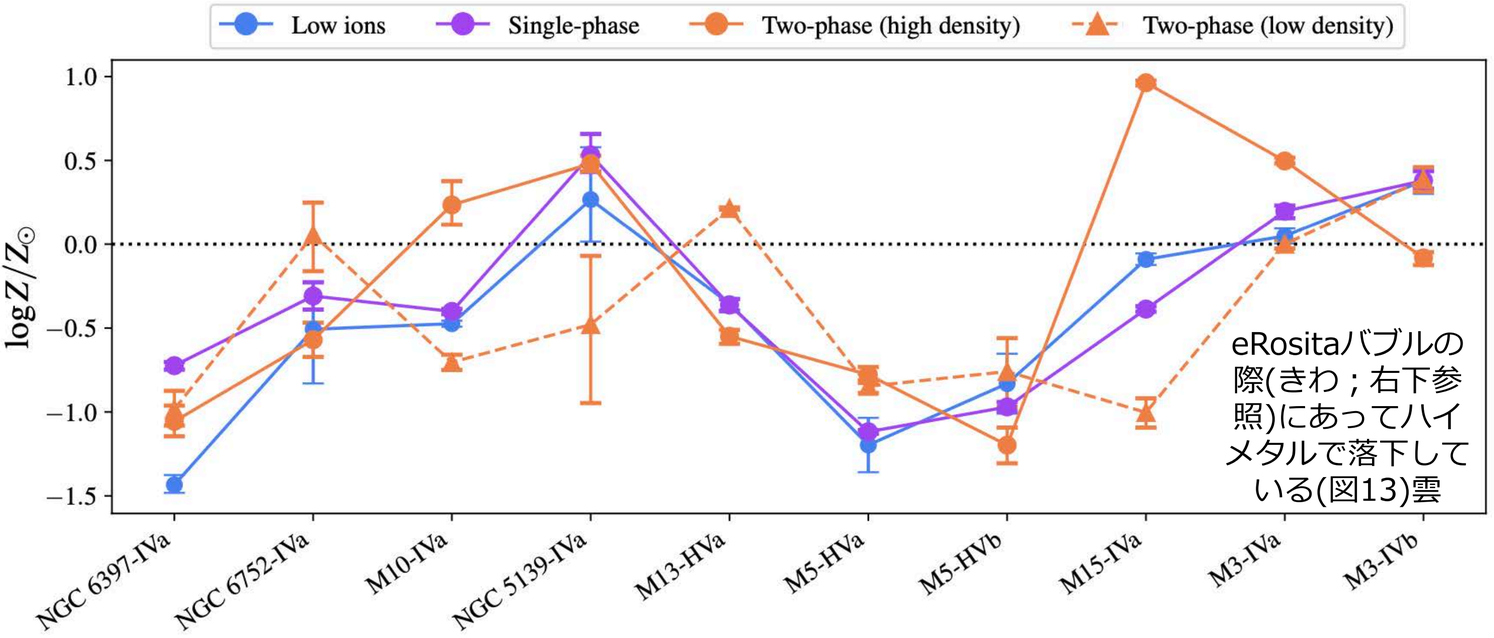

Figure 7. The metallicity comparison between photoionized cloud models. The errors are provided by the HMC PDF with 2σ confidence. The blue circle points are for "photoionized low-ion cloud", purple points represent "single-phase photoionized cloud", and orange points show "two-phase photoionized cloud" of which each density phase is noted with point shape and line style, circle points with solid line (high density) and triangle points with dashed line (low density). Solar metallicity $Z_\odot$ is marked with black dotted line.

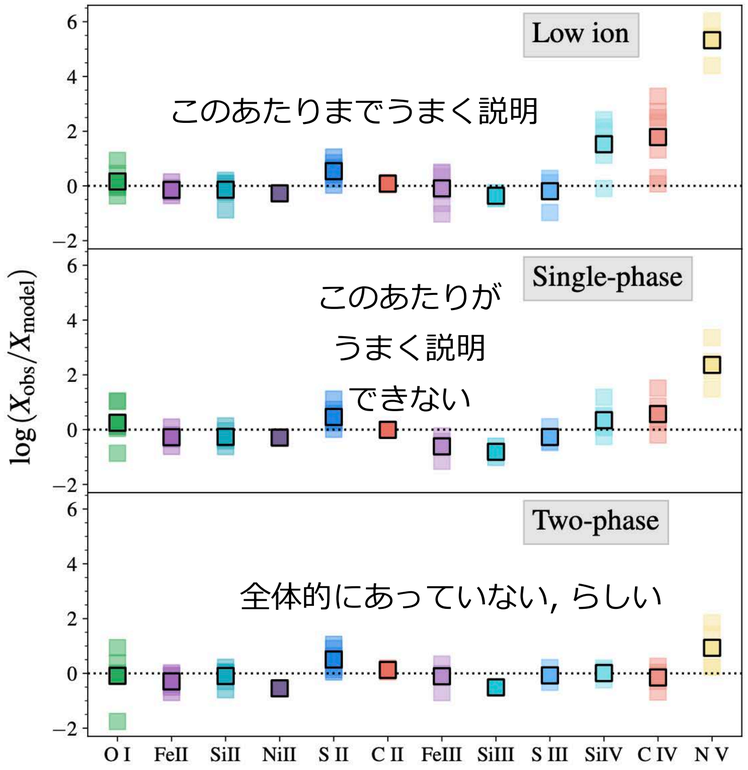

- **低イオン」モデル**：”低イオン”が光イオン化ガス相に存在し，中間および高イオンが衝突イオン化されている場合 (結局，このモデルがベストと判断)

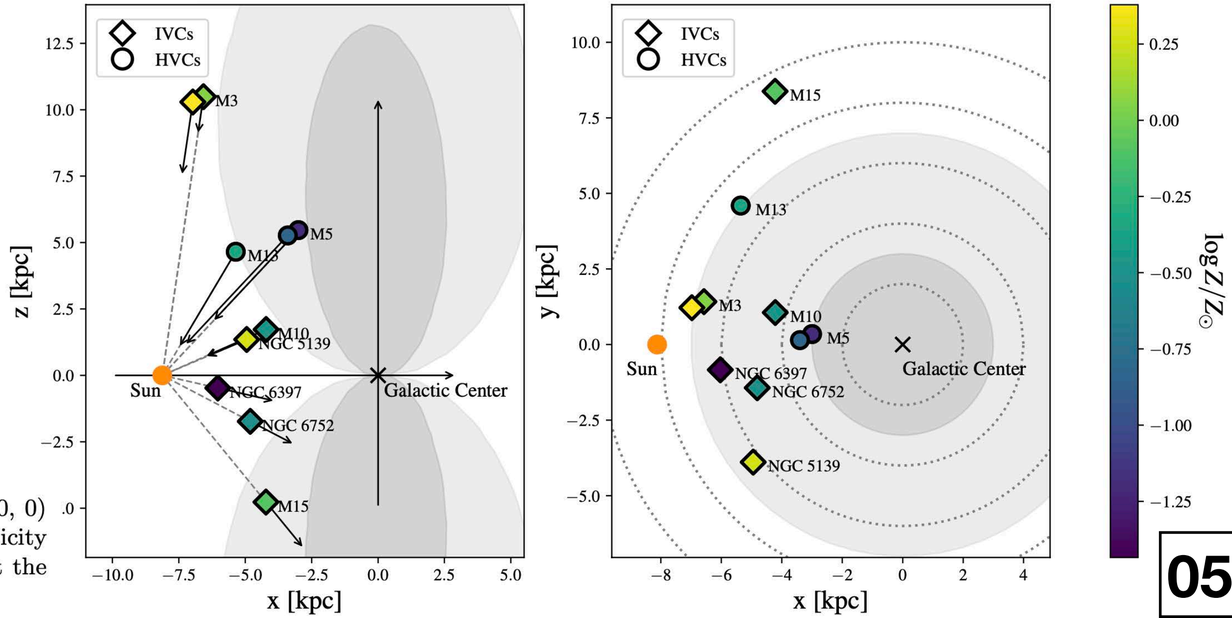

Figure 10. The detected IVCs (diamond) and HVCs (circle) in the Galactocentric system where the Sun is at (-8.122, 0, 0) kpc. The left panel shows the distribution in the XZ plane and the right panel is for the XY plane. We show our metallicity estimation in color. The vector sizes are proportional to the line of sight velocity centroids in the LSR. We also present the Fermi (dark gray-shaded) and eROSITA bubbles (gray-shaded) with their approximate size (Predehl et al. 2020).

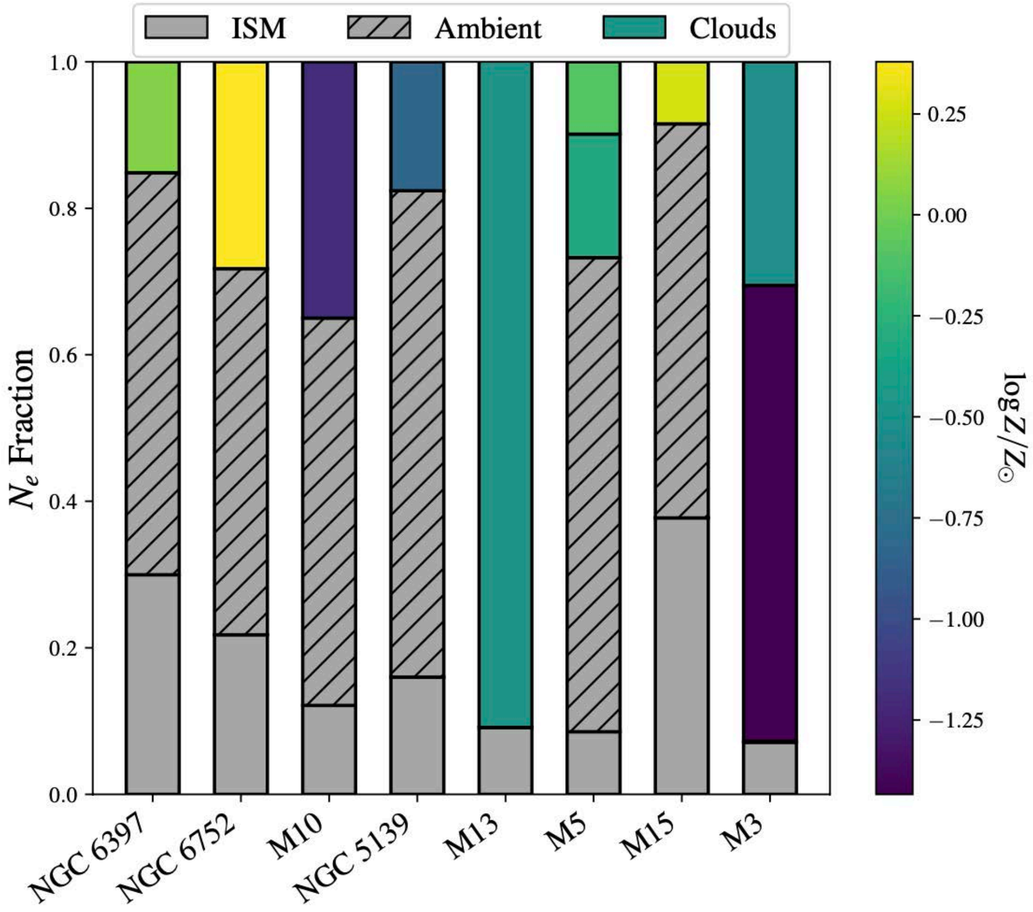

Figure 9. Bar chart showing the the electron column density, N_e, fraction for each gas component along the GC sight lines, ordered by increasing distance to the GCs. Each bar is divided into three components: Milky Way ISM (gray), clouds (color), and ambient (gray-hatched). The fraction of the bar representing the IVCs and HVCs is color-coded according to metallicity. The ISM fraction is calculated by the NE2001 model, as discussed in Section 4. The electron column density of each cloud is estimated from the HMC fitting with photoionization modeling. Since we set N_e given by the pulsar DMs as an upper limit, this allows for an additional component of electron column density besides that of the clouds and ISM, possibly ambient hot halo gas. The ambient gas is the dominant source of free electrons along most lines of sight.

それぞれの視線を構成する電子は,結局, どこにあったものか？
(ターゲット本体, その周囲, 太陽系から「その周囲」までの視線のどこにあったか？)
カラー部分の長さの比がターゲットの寄与；カラーはその金属量

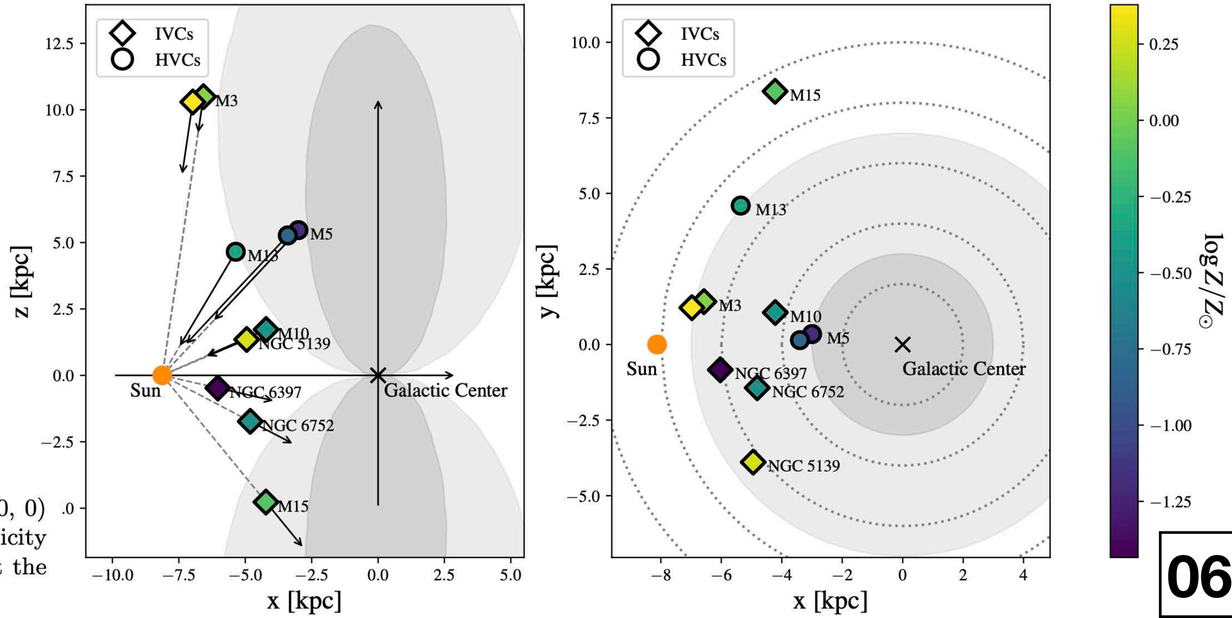

Figure 10. The detected IVCs (diamond) and HVCs (circle) in the Galactocentric system where the Sun is at (-8.122, 0, 0) kpc. The left panel shows the distribution in the XZ plane and the right panel is for the XY plane. We show our metallicity estimation in color. The vector sizes are proportional to the line of sight velocity centroids in the LSR. We also present the Fermi (dark gray-shaded) and eROSITA bubbles (gray-shaded) with their approximate size (Predehl et al. 2020).

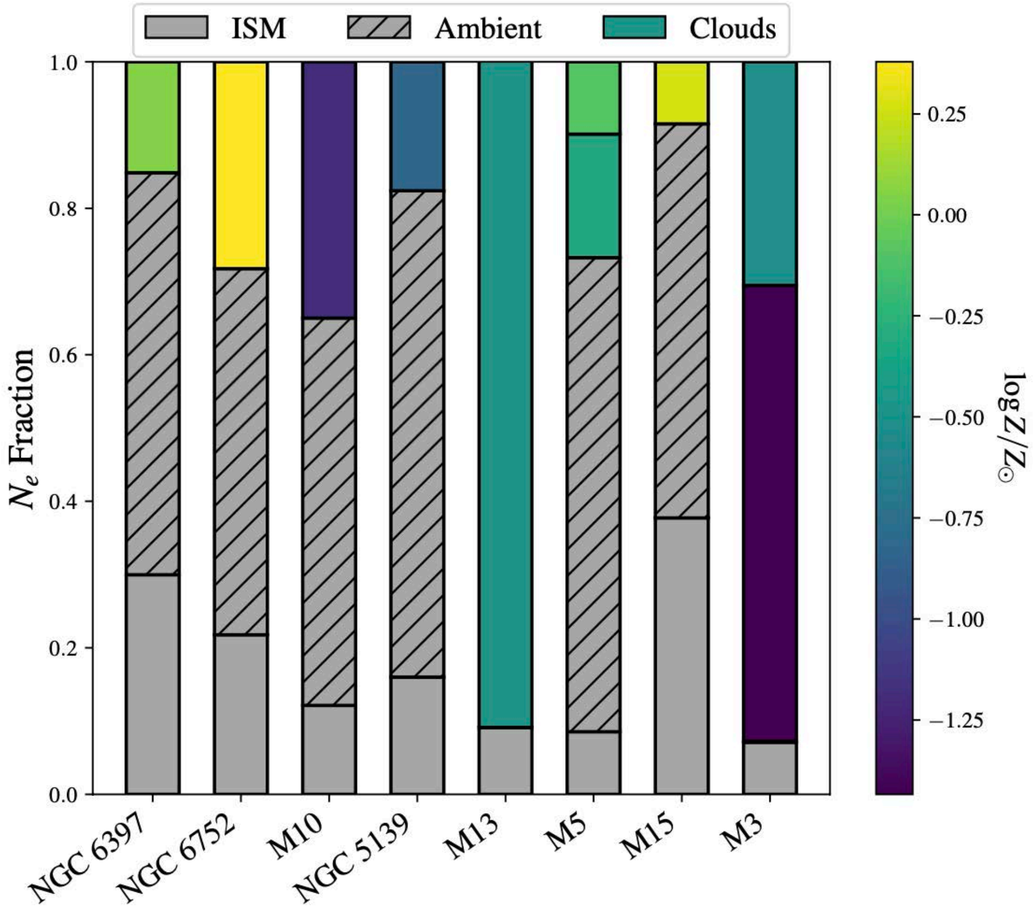

Figure 9. Bar chart showing the the electron column density, N_e, fraction for each gas component along the GC sight lines, ordered by increasing distance to the GCs. Each bar is divided into three components: Milky Way ISM (gray), clouds (color), and ambient (gray-hatched). The fraction of the bar representing the IVCs and HVCs is color-coded according to metallicity. The ISM fraction is calculated by the NE2001 model, as discussed in Section 4. The electron column density of each cloud is estimated from the HMC fitting with photoionization modeling. Since we set N_e given by the pulsar DMs as an upper limit, this allows for an additional component of electron column density besides that of the clouds and ISM, possibly ambient hot halo gas. The ambient gas is the dominant source of free electrons along most lines of sight.

それぞれの視線を構成する電子は,結局, どこにあったものか？
(ターゲット本体, その周囲, 太陽系から「その周囲」までの視線のどこにあったか？)
カラー部分の長さの比がターゲットの寄与；カラーはその金属量

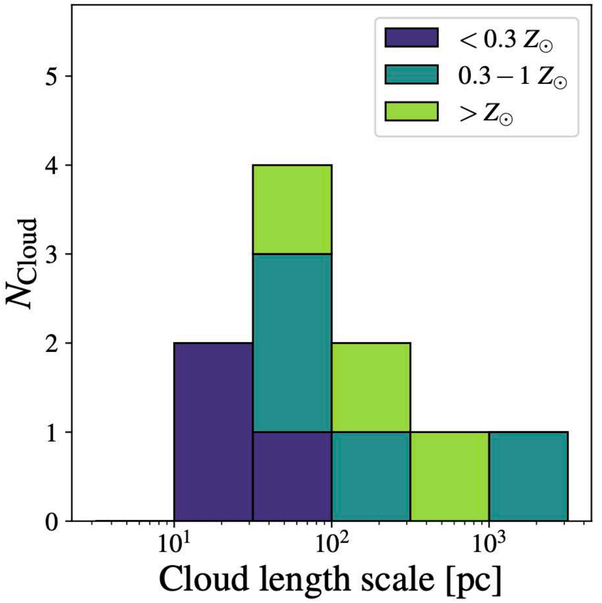

Figure 11. A histogram of cloud size. Most of the clouds have a size on the order of ∼ 100 pc. The color shows the three metallicity ranges, less than 0.3 $Z_\odot$ (blue), 0.3 - 1 $Z_\odot$ (purple), and super-solar (pink).

ターゲットの電子密度がわかっている(はず)なので,
ターゲット雲の奥行きがわかる, それがFig.11

$n_e = \frac{DM}{d}$ ← 雲までの距離

雲までの分散 σ_{ne}^2 は,

$\sigma_{ne}^2 = \left(\frac{\partial n_e}{\partial DM}\cdot\delta DM\right)^2 + \left(\frac{\partial n_e}{\partial d}\delta d\right)^2$

$= \left(\frac{\delta DM}{d}\right)^2 + \left(\frac{DM}{d^2}\delta d\right)^2$ ・・・(1)

DMの不定性の典型値は, 5%らしい.
仮りに雲までの不定性が 30%とすると,
$d = 1$ kpc, $DM = 100$ pc·cm^{-3} とすると, (1)式は,

$\sigma_{ne}^2 = 2.5\times10^{-5}$ cm^{-3} + 9×10^{-9} cm^{-3}

$\simeq 3\times10^{-5}$ cm^{-3} + 1×10^{-3} cm^{-3}

DMのエラーの寄与　雲までのエラー

雲までのエラーの寄与が支配的!!

ということがわかってしまったが,
この論文ではそこは触れていない.
まぁ, そういう論文だと頭に入れて残りを読む

しかし, 奥行きの「デカさ」を見ると
距離の影響は？という疑問が湧く.

Table 4. Kinematic model parameters.

Parameter	Inflow	Outflow	Stagnant
(km s^{-1})			
v_r	30^{+15}_{-11}	-22^{+39}_{-35}	0
v_ϕ	233 ± 18	232^{+91}_{-54}	200 ± 30
v_z	-67^{+8}_{-11}	-22^{+39}_{-35}	0

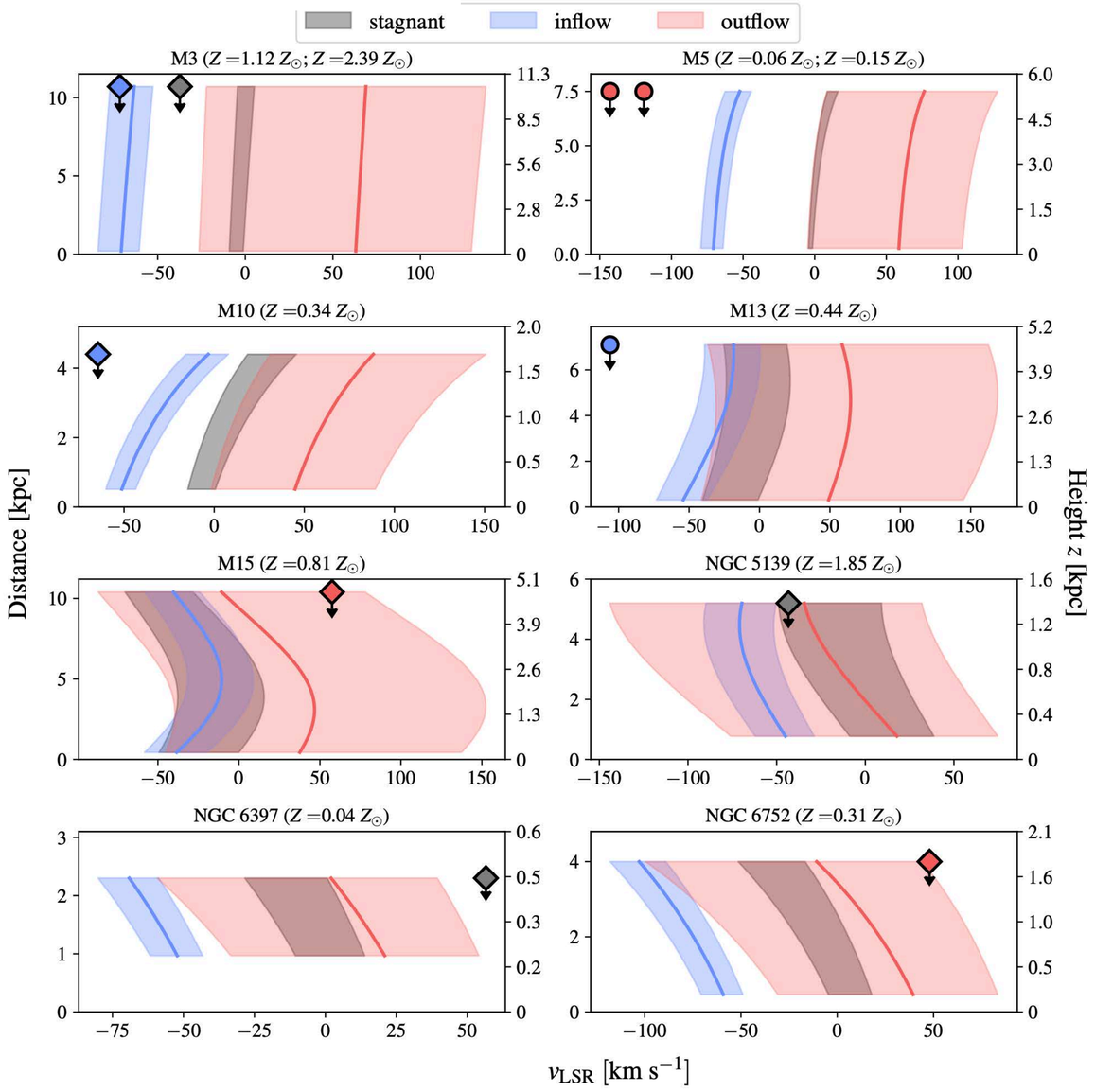

Figure 13. Kinematic modeling of LSR velocity for each sight line and observed LSR velocity of the detected IVCs (diamond) and HVCs (circle). LSR velocity is a function of distance from the Sun (left y-axis), and the maximum distance is given by the distance to the targeted halo stars. We present the predictions of inflow (blue-shaded), outflow (red-shaded), and stagnant (hatched) models with the parameters given in Table 4. The color of the data points denotes the categorization of inflow (blue), outflow (red), and ambiguous (gray).

The Metallicity Mapping of the Ionized Diffuse Gas at the Milky Way Disk-halo Interface

Bo-Eun Choi [1], Jessica K. Werk [1], Kirill Tchernyshyov [1], J. Xavier Prochaska [2,3,4], Yong Zheng [5], Mary E. Putman [6], Drummond B. Fielding [7,8] and Jay Strader [9]

[1] Department of Astronomy, University of Washington, Seattle, WA 98195, USA
[2] Department of Astronomy and Astrophysics, University of California, Santa Cruz, CA 95064, USA
[3] Kavli Institute for the Physics and Mathematics of the Universe (Kavli IPMU), 5-1-5 Kashiwanoha, Kashiwa, 277-8583, Japan
[4] Division of Science, National Astronomical Observatory of Japan, 2-21-1 Osawa, Mitaka, Tokyo 181-8588, Japan
[5] Department of Physics, Applied Physics and Astronomy, Rensselaer Polytechnic Institute, Troy, NY 12180
[6] Department of Astronomy, Columbia University, New York, NY 10027, USA
[7] Department of Astronomy, Cornell University, Ithaca, NY 14853, USA
[8] Center for Computational Astrophysics, Flatiron Institute, 162 Fifth Avenue, New York, NY 10010, USA
[9] Center for Data Intensive and Time Domain Astronomy, Department of Physics and Astronomy, Michigan State University, East Lansing, MI 48824, USA

ABSTRACT

Metals in the diffuse, ionized gas at the boundary between the Milky Way's interstellar medium (ISM) and circumgalactic medium (CGM), known as the disk-halo interface (DHI), are valuable tracers of the feedback processes that drive the Galactic fountain. However, metallicity measurements in this region are challenging due to obscuration by the Milky Way ISM and uncertain ionization corrections that affect the total hydrogen column density. In this work, we constrain the ionization corrections to neutral hydrogen column densities using precisely measured electron column densities from the dispersion measure of pulsars that lie in the same globular clusters as UV-bright targets with high-resolution absorption spectroscopy. We address the blending of absorption lines with the ISM by jointly fitting Voigt profiles to all absorption components. We present our metallicity estimates for the DHI of the Milky Way based on detailed photoionization modeling to the absorption from ionized metal lines and ionization-corrected total hydrogen columns. Generally, the gas clouds show a large scatter in metallicity, ranging between $0.04 - 3.2\ Z_\odot$, implying that the DHI consists of a mixture of gaseous structures having multiple origins. We estimate the inflow and outflow timescales of the DHI ionized clouds to be $6 - 35$ Myr. We report the detection of an infalling cloud with super-solar metallicity that suggests a Galactic fountain mechanism, whereas at least one low-metallicity outflowing cloud ($Z < 0.1\ Z_\odot$) poses a challenge for Galactic fountain and feedback models.

01

銀河系のDHIに対して，

1. パルサーDMでN_e^{total}
2. 紫外線吸収スペクトルから金属イオンのN
3. 光イオン化モデルで銀河系ISMとターゲット雲の電子密度を分離
4. 金属量推定
5. DHI中の構成雲の運動をモデル推定
6. さまざまな金属量のDHI構成ガスが銀河系内の物質循環とCGMとの物質交換に果たす役割を議論

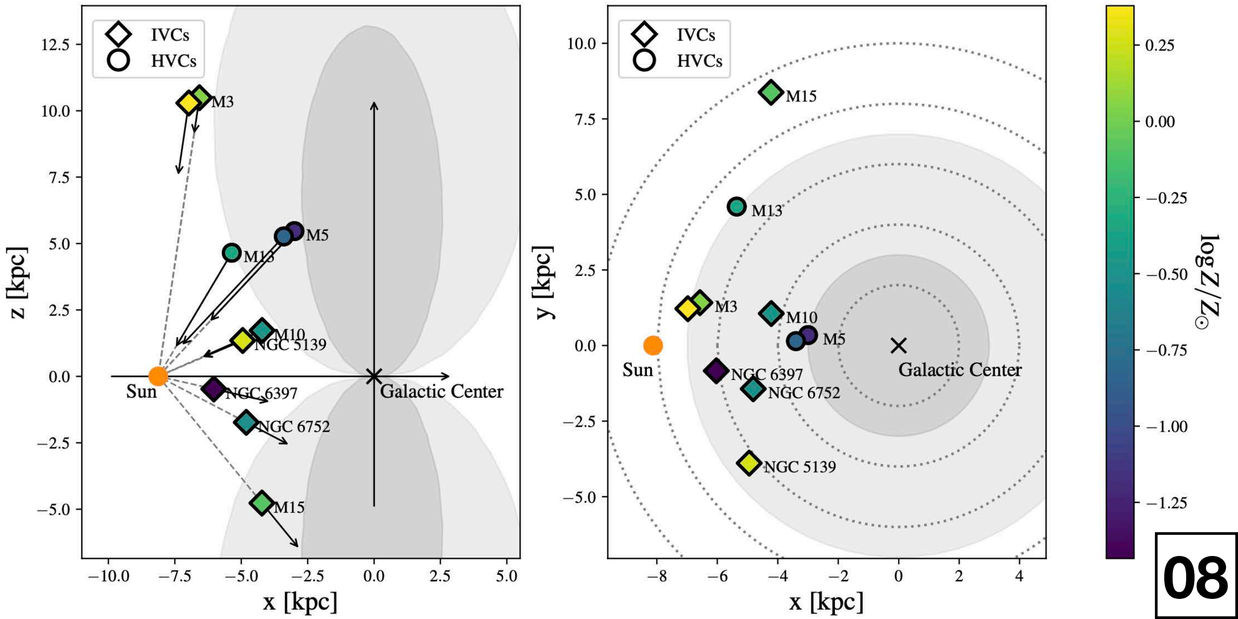

08

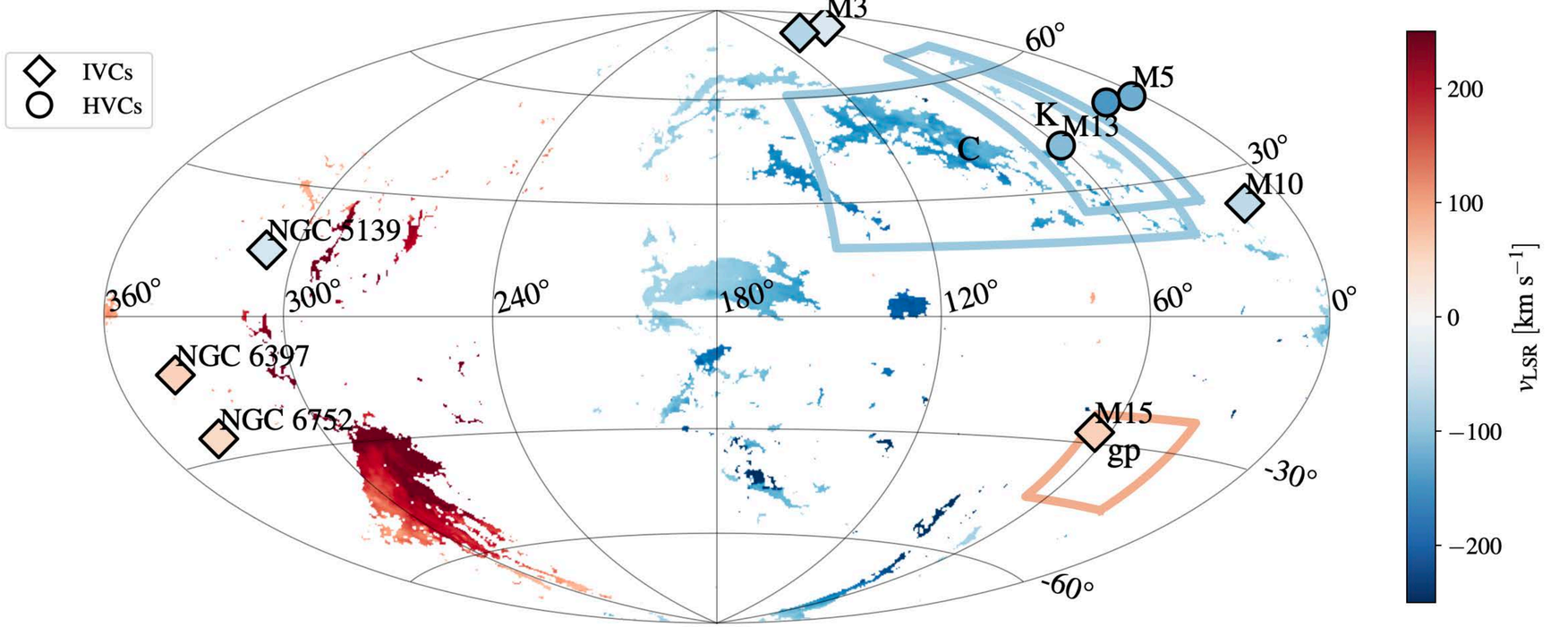

(a) The Galactic distribution of detected IVCs (diamond) and HVCs (circle) with an all-sky H I velocity map from the 21-cm HI4PI survey (Westmeier 2018). Our clouds are potentially part of the known IVC and HVC complexes, Complex C, Complex K, and Complex gp. The three complexes are presented with boxed outlines having a color corresponding to their average LSR velocity.

この研究の新しさ

従来の定説と違い, **現実は複雑である**ことを**それなりの数のサンプル**をもとに**同じ手法の解析で**初めて示したこと.

これまでの定説は, 「うまく行った」個別観測&個別解析を組み合わせて, IVCは1-2kpcのnear solar metalで銀河系中心からの噴出現象起源, HVCは<10-15 kpcでlow metalでIGM起源の可能性もあり, だった.

ただし, この研究はあくまでもペンシルビームでの定量 (星印の視線)

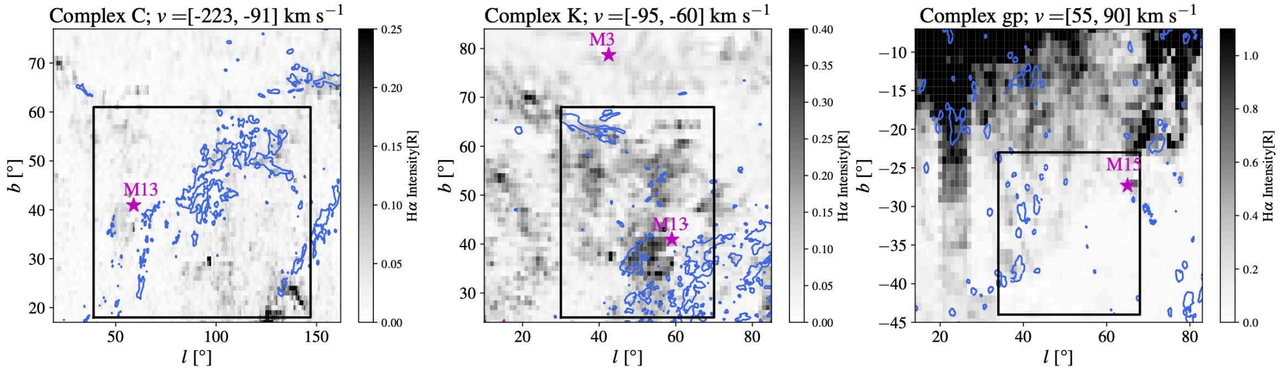

(b) The WHAM map for Complex C (left), Complex K (center), and Complex gp (right). The black boxes correspond to the location of the known complexes. The Hα intensity is integrated for the LSR velocity ranges of each complex, presented on top of the map. The LSR velocity ranges are referred to van Woerden et al. (2004). We note that the WHAM survey covers the velocity range of roughly $(-100, 100)$ km s^{-1}, thus it only covers a small fraction of the velocity range of Complex C. The range of intensities varies for each map, as indicated by the corresponding color bar. The H I map from the HI4PI survey (HI4PI Collaboration et al. 2016) is presented with blue contours with the column density of $N_{\rm HI} = 10^{19.5}, 10^{19}$, and 10^{18} cm^{-2} for Complex C, Complex K, and Complex gp, respectively. We show the location of our three sight lines that are potentially associated with the complexes (magenta stars).

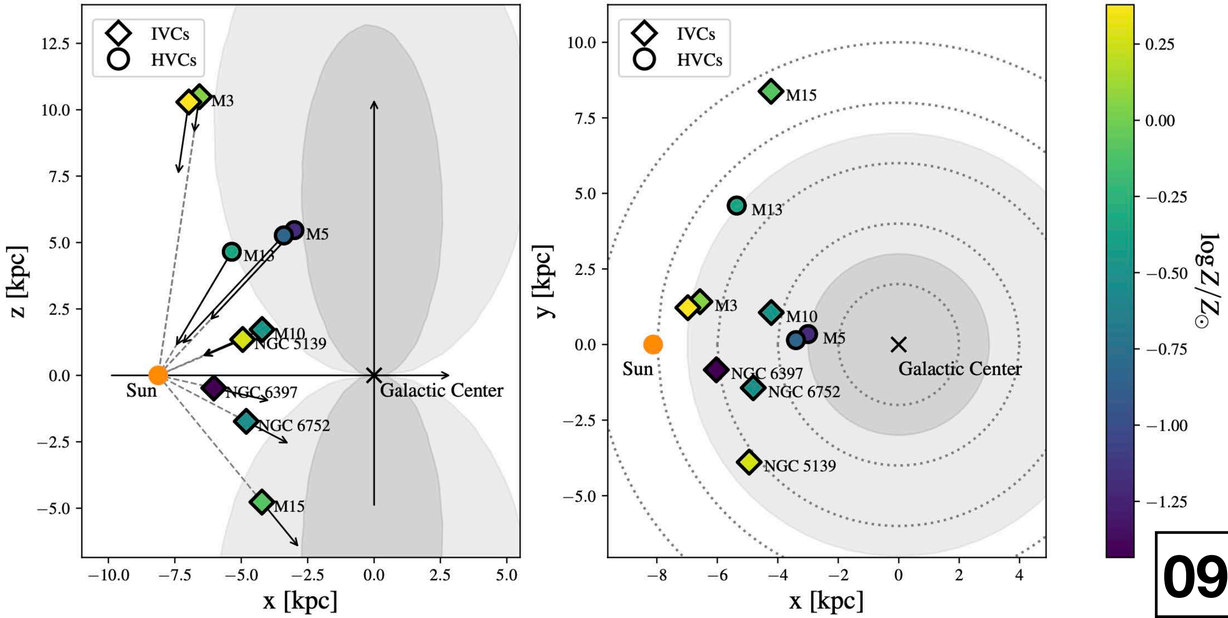

Cosmic Ray-Driven Galactic Winds with Resolved ISM and Ion-Neutral Damping

Brandon Sike [1], Timon Thomas [2], Mateusz Ruszkowski [1], Christoph Pfrommer [2] and Matthias Weber [2]

[1] *Department of Astronomy, University of Michigan, Ann Arbor, MI 48109, USA*
[2] *Leibniz Institute for Astrophysics, Potsdam (AIP), An der Sternwarte 16, D-14482 Potsdam, Germany*

ABSTRACT

Feedback processes in galaxies dictate their structure and evolution. Baryons can be cycled through stars, which inject energy into the interstellar medium (ISM) in supernova explosions, fueling multiphase galactic winds. Cosmic rays (CRs) accelerated at supernova remnants are an important component of feedback. CRs can effectively contribute to wind driving; however, their impact heavily depends on the assumed CR transport model. We run high-resolution "tallbox" simulations of a patch of a galactic disk using the moving mesh magnetohydrodynamics code Arepo, including varied CR implementations and the Crisp non-equilibrium thermochemistry model. We characterize the impact of CR feedback on star formation and multiphase outflows. While CR-driven winds are able to supply energy to a global-scale wind, a purely thermal wind loses most of its energy by the time it reaches 3 kpc above the disk midplane. We further find that the adopted CR transport model significantly affects the steady-state of the wind. In the model with CR advection, streaming, diffusion, and nonlinear Landau damping, CRs provide very strong feedback. Additionally accounting for ion-neutral damping (IND) decouples CRs from the cold ISM, which reduces the impact of CRs on the star formation rate. Nevertheless, CRs in this most realistic model are able to accelerate warm gas and levitate cool gas in the wind but have little effect on cold gas and hot gas. This model displays moderate mass loading and significant CR energy loading, demonstrating that IND does not prevent CRs from providing effective feedback.

銀河系の鉛直方向に関する金属量分布を説明するモデルの論文；円盤内のメタル分布を与え, それを力学的な作用(e.g.,銀河噴水)ではなく, 宇宙線密度の勾配力で噴き上げるモデルらしい.

Paper I

Galaxy Evolution in The Post-Merger Regime I – Most merger-induced in-situ stellar mass growth happens post-coalescence

Leonardo Ferreira[1],[⋆] Sara L. Ellison[1], David R. Patton[2], Shoshannah Byrne-Mamahit[1], Scott Wilkinson[1], Robert Bickley[1], Christopher J. Conselice[3], Connor Bottrell[4]
[1] *School of Physics and Astronomy, University of Victoria, Victoria, BC, Canada*
[2]*Department of Physics and Astronomy, Trent University, 1600 West Bank Drive, Peterborough, ON K9L 0G2, Canada*
[3]*Jodrell Bank Centre for Astrophysics, University of Manchester, Oxford Road, Manchester UK*
[4]*International Centre for Radio Astronomy Research, University of Western Australia, 35 Stirling Hwy, Crawley, WA 6009, Australia*

主題：クエンチングのタイミングと機構

手法：サーベイ観測とシミュレーション

結果：星形成を抑制する機構は多様な要因が相互作用；特に乱流とフィードバック

Paper II

GALAXY EVOLUTION IN THE POST-MERGER REGIME. II - POST-MERGER QUENCHING PEAKS WITHIN 500 MYR OF COALESCENCE

Sara L. Ellison[1], Leonardo Ferreira[1], Vivienne Wild[2], Scott Wilkinson[1], Kate Rowlands[3], and David R. Patton[4]
[1] Department of Physics & Astronomy, University of Victoria, Finnerty Road, Victoria, BC V8P 1A1, Canada
[2] School of Physics and Astronomy, University of St Andrews, North Haugh, St Andrews, KY16 9SS, U.K.
[3] AURA for ESA, Space Telescope Science Institute, 3700 San Martin Drive, Baltimore, MD 21218, USA
[4] Department of Physics and Astronomy, Trent University, 1600 West Bank Drive, Peterborough, ON K9L 0G2, Canada
Version October 11, 2024

主題：ポストスターバースト(PSB)に焦点をあて, 合体後, いつ星形成が急速に停止するのか？

手法：サーベイ観測データセットと機械学習モデル, クエンチングの時系列解析

結果：星形成が停止するタイミングには合体後0.2-0.5Gyrという特徴的な時間がある.

MNRAS 000, 1–6 (2024) Preprint 10 October 2024 Compiled using MNRAS LATEX style file v3.3

Galaxy Evolution in The Post-Merger Regime I – Most merger-induced in-situ stellar mass growth happens post-coalescence

Leonardo Ferreira[1],★ Sara L. Ellison[1], David R. Patton[2], Shoshannah Byrne-Mamahit[1], Scott Wilkinson[1], Robert Bickley[1], Christopher J. Conselice[3], Connor Bottrell[4]

[1] School of Physics and Astronomy, University of Victo
[2]Department of Physics and Astronomy, Trent Universi
[3]Jodrell Bank Centre for Astrophysics, University of M
[4]International Centre for Radio Astronomy Research, U

Accepted XXX. Received YYY; in original form ZZZ

主な結果

合体から500 Myr以内のクエンチングがピークに達する：合体後0.16～0.48 Gyrの範囲で, PSBの割合がコントロールサンプルの30～100倍になるので, この期間がクエンチングの最も顕著と主張

星形成の進化：合体後はスターバーストするが, 時間が経つにつれて星形成率は低下し, 最終的に1 Gyr後にはメインシークエンス銀河に比べても顕著にクエンチングが支配的.

近傍宇宙のPSB銀河の多くが, 実は合体の結果ではないかという主張：全PSBの約75%（ある選択基準）および約61%（別の基準）が, 銀河合体と関連あるいはその直接的結果

ABSTRACT

Galaxy mergers can enhance star formation rates throughout the merger sequence, with this effect peaking around the time of coalescence. However, owing to a lack of information about their time of coalescence, post-mergers could only previously be studied as a single, time-averaged population. We use timescale predictions of post-coalescence galaxies in the UNIONS survey, based on the Multi-Model Merger Identifier deep learning framework (Mummi) that predicts the time elapsed since the last merging event. For the first time, we capture a complete timeline of star formation enhancements due to galaxy mergers by combining these post-merger predictions with data from pre-coalescence galaxy pairs in SDSS. Using a sample of 564 galaxies with $M_* \geq 10^{10} M_\odot$ at $0.005 < z < 0.3$ we demonstrate that: 1) galaxy mergers enhance star formation by, on average, up to a factor of two; 2) this enhancement peaks within 500 Myr of coalescence; 3) enhancements continue for up to 1 Gyr after coalescence; and 4) merger-induced star formation significantly contributes to galaxy mass assembly, with galaxies increasing their final stellar masses by, 10% to 20% per merging event, producing on average $\log(M_*/M_\odot) = 9.56^{+0.13}_{-0.19}$ more mass than non-interacting star-forming galaxies solely due to the excess star formation.

Key words: methods: data analysis – galaxies: evolution – galaxies: interactions.

GALAXY EVOLUTION IN THE POST-MERGER REGIME. II - POST-MERGER QUENCHING PEAKS WITHIN 500 MYR OF COALESCENCE

Sara L. Ellison[1], Leonardo Ferreira[1], Vivienne Wild[2], Scott Wilkinson[1], Kate Rowlands[3], and David R. Patton[4]

[1] Department of Physics & Astronomy, University of Victoria, Finnerty Road, Victoria, BC V8P 1A1, Canada
[2] School of Physics and Astronomy, University of St Andrews, North Haugh, St Andrews, KY16 9SS, U.K.
[3] AURA for ESA, Space Telescope Science Institute, 3700 San Martin Drive, Baltimore, MD 21218, USA
[4] Department of Physics and Astronomy, Trent University, 1600 West Bank Drive, Peterborough, ON K9L 0G2, Canada

Version October 11, 2024

ABSTRACT

Mechanisms for quenching star formation in galaxies remain hotly debated, with galaxy mergers an oft-proposed pathway. In Ellison et al. (2022) we tested this scenario by quantifying the fraction of recently and rapidly quenched post-starbursts (PSBs) in a sample of post-merger galaxies identified in the Ultraviolet Near Infrared Optical Northern Survey (UNIONS). Compared with a control sample of non-interacting galaxies, Ellison et al. (2022) found PSBs to be a factor of 30-60 more common in the post-mergers, demonstrating that mergers can lead to quenching. However, the exact timing of this post-merger quenching was unconstrained. Thanks to our recent development of the Multi-Model Merger Identifier (MUMMI) neural network ensemble (Ferreira et al. 2024a,b), we are now able to predict the time since coalescence (T_{PM}) for the UNIONS post-merger galaxies up to $T_{PM} = 1.8$ Gyr, allowing us to further dissect the merger sequence and measure more precisely when quenching occurs. Based on a sample of 5927 $z < 0.3$ post-mergers identified in UNIONS, we find that the post-coalescence population evolves from one dominated by star-forming (and starbursting) galaxies at $0 < T_{PM} < 0.16$ Gyr, through to a population that is dominated by quenched galaxies by $T_{PM} \sim 1.5$ Gyr. By combining the post-mergers with a sample of 15,831 spectroscopic galaxy pairs with projected separations $r_p < 100$ kpc we are able to trace the evolution of quenching during the full merger sequence. We find a PSB excess throughout the post-merger regime, but with a clear peak at $0.16 < T_{PM} < 0.48$ Gyr. In this post-merger time range PSBs are more common than in control galaxies by factors of 30-100 (depending on PSB selection method), an excess that drops sharply at longer times since merger. We also quantify the fraction of PSBs that are mergers and find that the majority (75 per cent) of classically selected E+A are identified as either pairs or post-mergers, with a lower merger fraction (60 per cent) amongst PCA selected PSBs. The merger fraction of PSB galaxies also correlates strongly with stellar mass. Taken together, our results demonstrate that 1) galaxy-galaxy interactions can lead to rapid post-merger quenching within 0.5 Gyr of coalescence, 2) the majority of (but not all) PSBs at low z are linked to mergers and 3) quenching pathways are diverse, with different PSB selection techniques likely identifying galaxies quenched by different physical processes with an additional dependence on stellar mass.

イントロの合体銀河を同定する試みの歴史的変遷の記述も興味深い(なぜこの研究が可能になったかの背景説明)

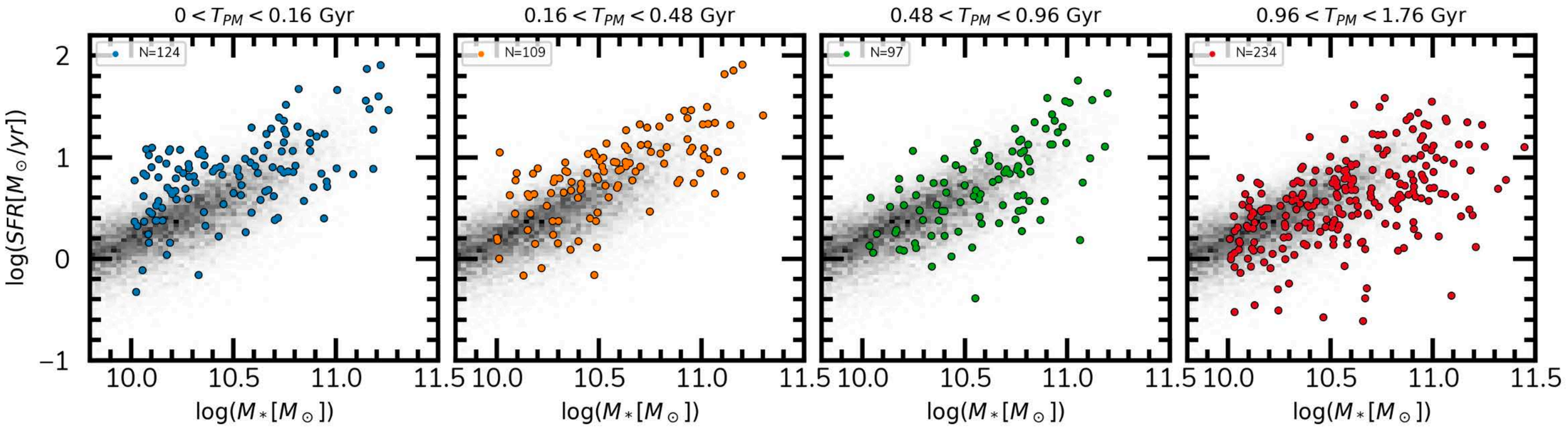

Figure 1. SFR vs. stellar mass of the post-merger sample. Each panel shows the distribution of SFRs and stellar masses for the corresponding time bin in our post-merger sample in coloured points, with $0 < T_{PM} < 0.16$ Gyr in blue, $0.16 < T_{PM} < 0.48$ in orange, $0.48 < T_{PM} < 0.96$ in green, and $0.96 < T_{PM} < 1.76$ in red, respectively. We plot in the background as a gray 2D histogram the complete control pool of MUMMI non-mergers to be matched to the post-merger sample, representing the star forming main sequence. It is clear that the shortest timescales exhibit the highest positive offsets.

この論文でのSFRの求め方：(1) Hα, (2)クエンチングし始めた銀河を含むので, 4000 Åブレイク(CaとFeの吸収線), (3)静止系UV可視スペクトルから中心でのSFR推定し, 銀河全体の色($g' - r$)とSFRの関係を利用して補正

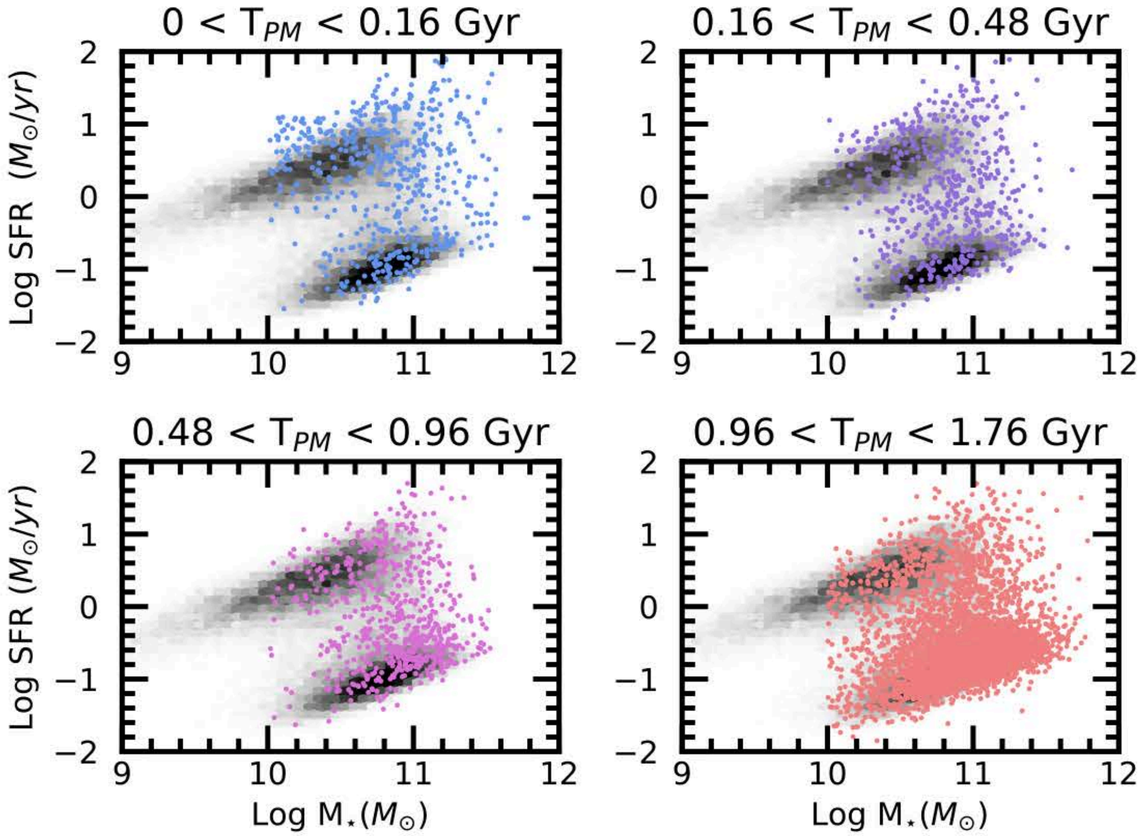

FIG. 3.— Star formation rate vs. stellar mass for the four T_{PM} bins in our sample. The greyscale in each panel shows the distribution of SFR and $M_\star$ for non-merger control pool galaxies in the UNIONS MUMMI sample. Coloured points show the post-merger galaxies. As time progresses since coalescence (i.e. increasing T_{PM}) the SFR demographics evolve from a population dominated by highly star-forming galaxies at short T_{PM} towards a high fraction in the green valley at intermediate times, before quenched galaxies dominate by 1 Gyr post-merger.

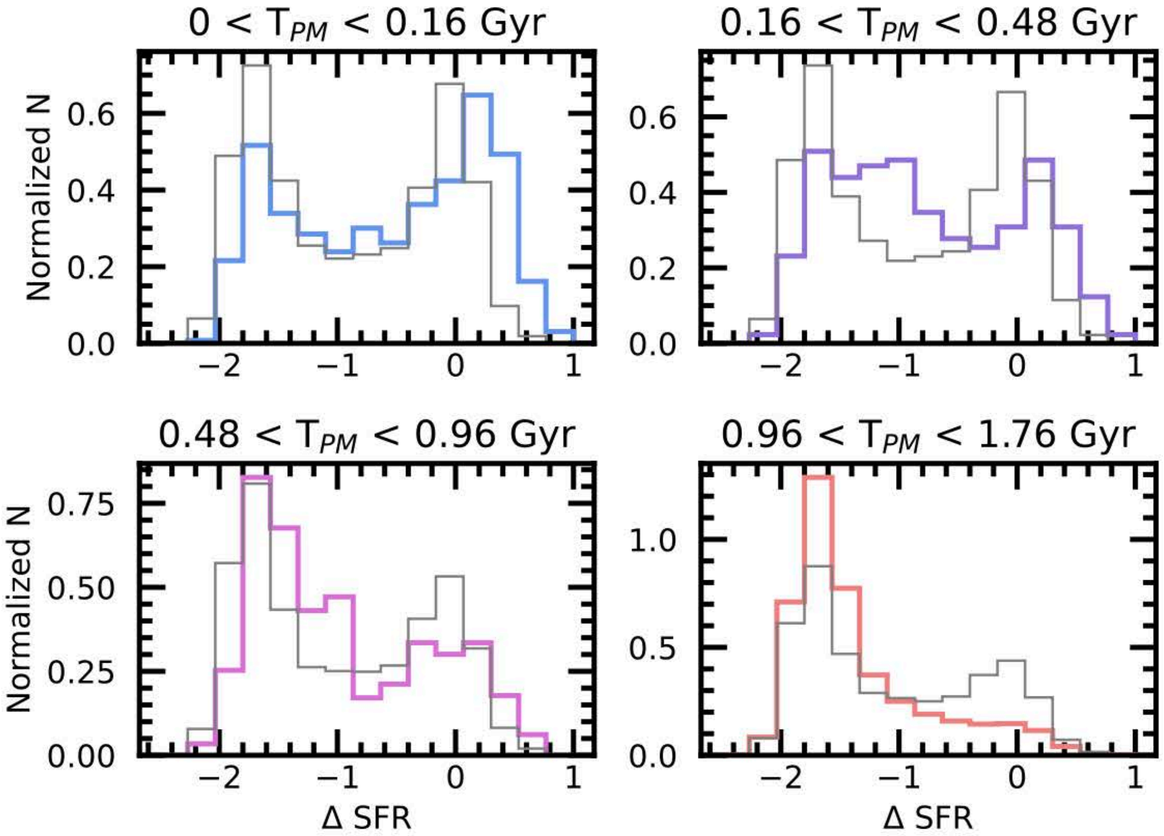

FIG. 4.— Distribution of Δ SFR for post-mergers in four time bins. In each panel the grey histogram is the control sample for a given time bin and the coloured line shows the post-mergers. At early times, post-mergers show an excess of star-forming galaxies and an elevated fraction of starbursts. As time progresses, the post-merger becomes dominated first by green valley galaxies at intermediate times, and then by quenched galaxies by $0.98 < T_{PM} < 1.76$ Gyr.

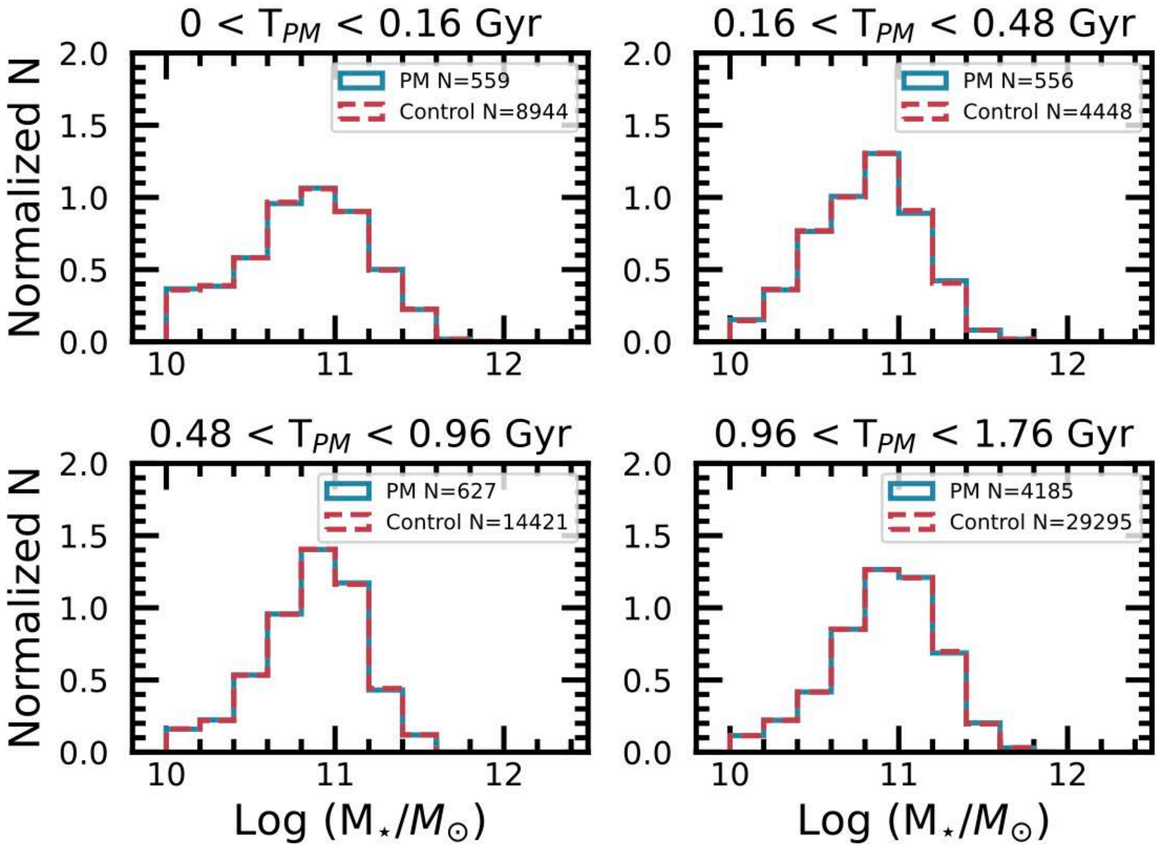

FIG. 1.— The stellar mass distributions of the post-merger sample in the four T_{PM} time bins (blue) and matched control sample (red dashed).

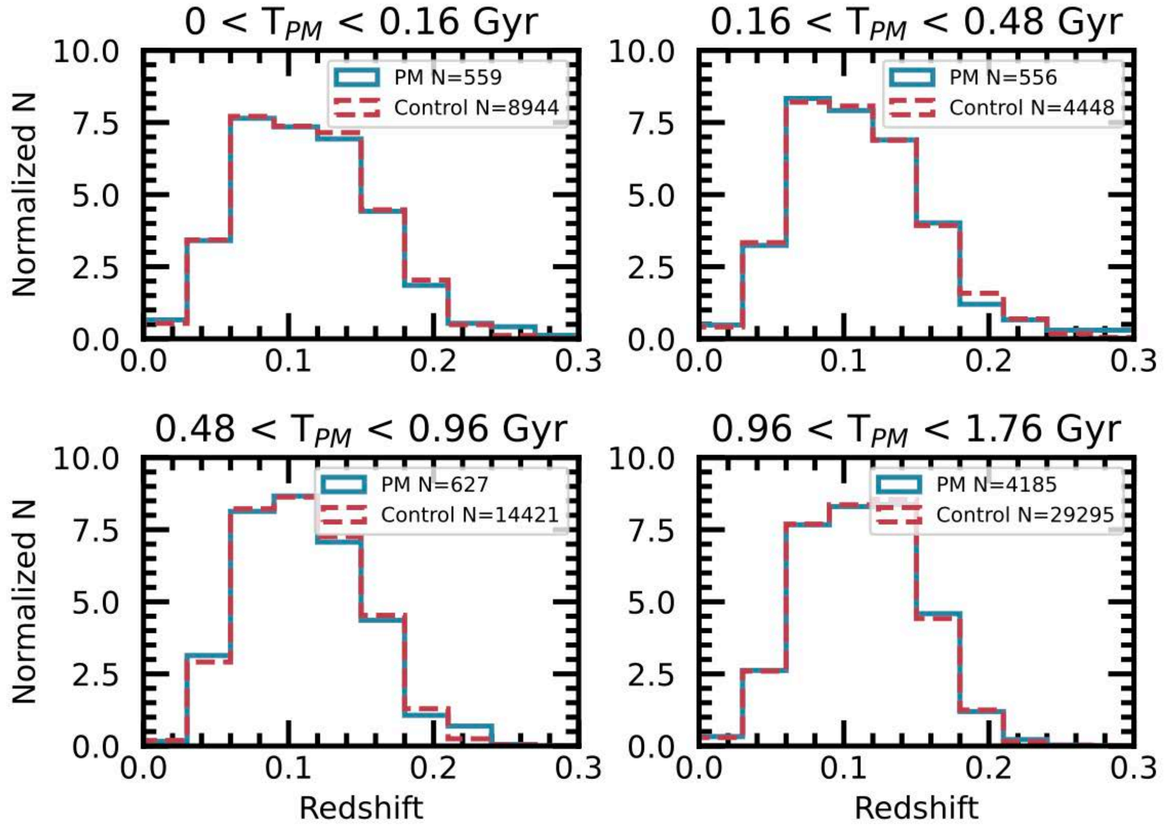

FIG. 2.— The redshift distributions of the post-merger sample in the four T_{PM} time bins (blue) and matched control sample (red dashed).

「銀河合体による星形成は, 銀河の星質量増加に大きく寄与する.」を主張する次の図の根拠の図

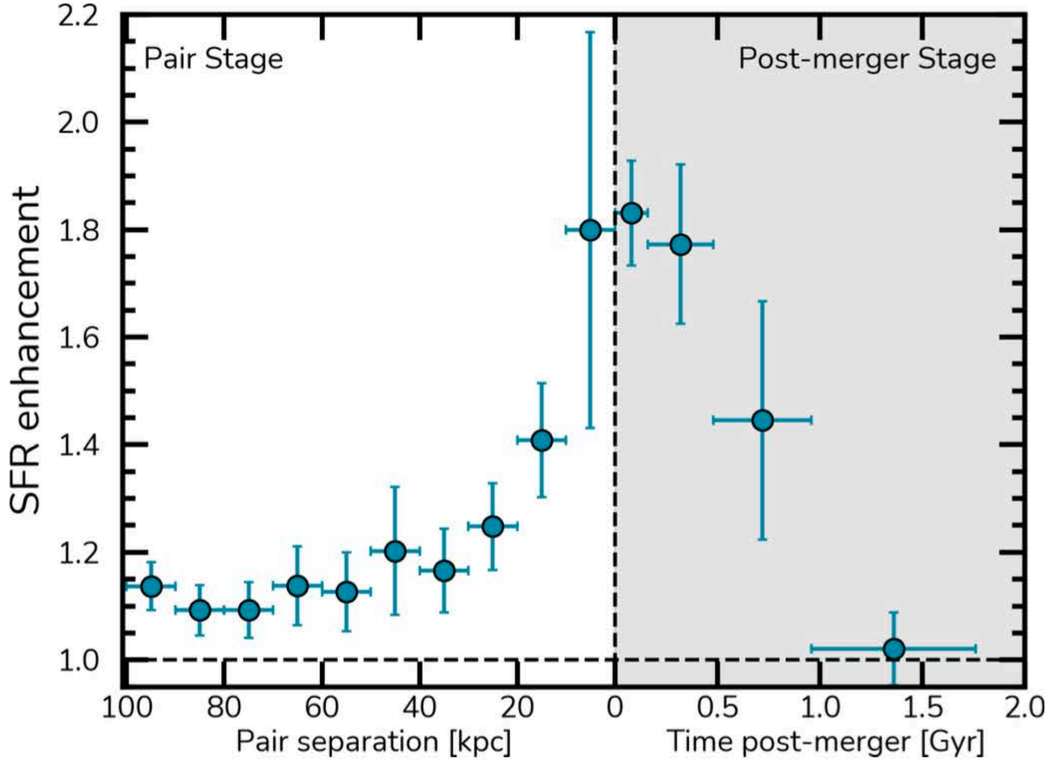

Figure 2. SFR Enhancements along the merger sequence. We show the evolution of SFR enhancements in the pair stage (left) and post-merger stage (right). For the pairs, we use their proximity as a proxy for a time until merger, while for post-mergers we use MUMMI timescale predictions. Galaxies display increasing enhanced SFRs with decreasing proximity with their companions, with this effect peaking at around the time of coalesence. SFRs can be enhanced as much as 2x when compared to selected controls. In the post-merger phase, these enhancements decay rapidly over a 1 Gyr time window, going back to normal at $0.96 < T_{PM} < 1.76$.

銀河合体は, 平均して最大2倍ほどのSFRの増加を引き起こし,
星形成が盛んな時期は最大で合体後1 Gyr続く.

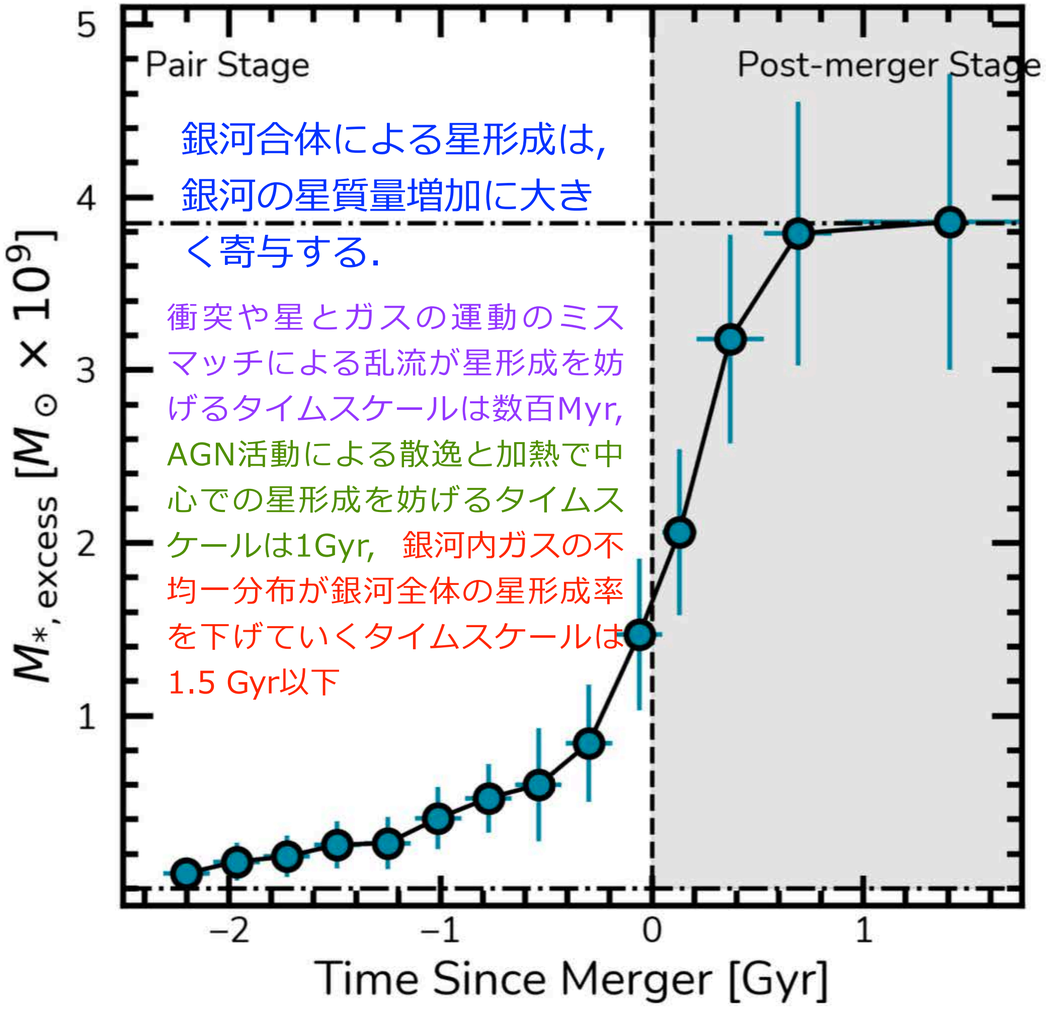

Figure 3. Cumulative Mass Formed along the merger sequence. We show how much cumulative stellar mass (current bin plus previous ones) is formed due to the enhanced star-formation along the complete merger sequence for all our sample. Merger-induced star-formation can form around $10^9 M_\odot$ by the end of the pair phase, and $10^{9.56} M_\odot$ in total by the end of the post-merger phase. This means that most mass formed due to enhancements from mergers are formed during the post-merger phase.